Accurate Modeling of GaN HEMTs Oriented to Analysis of Kink Effects in S_{22} and h_{21}: An Effective Machine Learning Approach

ZEGEN ZHU[1] (Student Member, IEEE), GIANNI BOSI[2] (Member, IEEE), ANTONIO RAFFO [2] (Member, IEEE), GIOVANNI CRUPI [3] (Senior Member, IEEE), AND JIALIN CAI [1] (Senior Member, IEEE)

1 Key Laboratory of RF Circuit and System, Ministry of Education, College of Electronics and Information, Hangzhou Dianzi University, Hangzhou 310018, China
2 Department of Engineering, University of Ferrara, 44122 Ferrara, Italy
3 BIOMORF Department, University of Messina, 98125 Messina, Italy

CORRESPONDING AUTHOR: J. CAI (e-mail: caijialin@hdu.edu.cn)

ABSTRACT In this work, for the first time, a machine learning behavioral modeling methodology based on gate recurrent unit (GRU) is developed and used to model and then analyze the kink effects (KEs) in the output reflection coefficient (S_{22}) and the short-circuit current gain (h_{21}) of an advanced microwave transistor. The device under test (DUT) is a 0.25-μm gallium nitride (GaN) high electron mobility transistor (HEMT) on silicon carbide (SiC) substrate, which has a large gate periphery of 1.5 mm. The scattering (S-) parameters of the DUT are measured at a frequency up to 65 GHz and at an ambient temperature up to 200°C. The proposed model can accurately reproduce the KEs in S_{22} and in h_{21}, enabling an effective analysis of their dependence on the operating conditions, bias point and ambient temperature. It is worth noticing that the proposed transistor model shows also good performance in both interpolation and extrapolation test.

INDEX TERMS GaN HEMT, GRU, kink effect, machine learning methods, semiconductor device modeling, scattering parameter measurements, temperature.

I. INTRODUCTION

In the last decade, the rapidly expanding of wireless communication market has stimulated the development of transistor technologies. The gallium nitride (GaN) high electron mobility transistor (HEMT) represents one of the most prevalent for the design of high-power amplifiers (HPAs) and low-noise amplifiers (LNAs) for application in the wireless communication industry [1], [2], since its outstanding qualities (e.g., high breakdown voltage and high electron saturation velocity) [3].

Accurate small-signal modeling of GaN HEMT technology is essential to build both large-signal and noise models [4], [5], [6], which are required for efficient HPA and LNA design [7], [8], [9]. Recently, some abnormal phenomena observed in its small-signal behavior have gained much attention, including the kink effects (KEs) [10], [11], [12], [13], [14], [15], [16], [17], [18], [19], [20], [21], [22]

in the output reflection coefficient (S_{22}) and in the short-circuit current gain (h_{21}) [14], [17], [23], [24], [25], [26], [27], [28].

In particular, the KE in S_{22} consists in a sudden change in the frequency-dependent behavior of S_{22} in the Smith chart, leading to significant adverse effects on output matching networks [10], [12]. On the other hand, the KE in h_{21} consists in a sudden increase in the magnitude of h_{21} in dB versus frequency on a logarithmic scale, that can allow achieving a sudden increase in the current gain and, then, is known as current-gain peak [23].

Different approaches have been explored to investigate the KEs. The most frequently used approach is based on providing a clear understanding of the KEs in S_{22} and in h_{21} in terms of the equivalent-circuit elements, thereby allowing one to establish the elements that play a dominant role, depending on the case under consideration. However, this

approach has the drawback of requiring the extraction of an equivalent-circuit model (ECM) and of being strictly dependent on the specific equivalent-circuit topology used for modeling the studied device [25].

In the recent years, a systematic and numerical methodology has been developed to characterize the size and the shape of the KEs in S_{22} [13], [14], [15] and in h_{21} [14] by using the second derivative (D2) of the functions $\text{Im}(S_{22})$ versus $\text{Re}(S_{22})$ and magnitude of h_{21} in dB versus the frequency, respectively. This approach allows defining a set of kink parameters to fully and mathematically quantify the KEs. However, owing to the high sensitivity to noise of the second derivative, trustworthy values of the kink parameters cannot be calculated directly from the measurements. Therefore, this approach needs the determination of fitting functions or model simulations (e.g., equivalent-circuit model and behavioral model) resembling the measured data in order to obtain a smooth behavior of D2 and, then, trustworthy values for the kink parameters. With the rapid development of machine learning (ML) [29], [30], [31], [32], [33], [34], it has become one of the most effective tools for behavioral modeling. Gate recurrent unit (GRU) is served as an efficient method for modeling as its exceeding capability of solving issues like vanishing and exploding gradients [35]. Compared with long short-term memory (LSTM) networks, GRU produces less parameters in model training process, thus making the modeling process more efficient.

In this paper, for the first time, a GRU-based model is developed to reproduce and, then, to study the small-signal behavior of the device under test (DUT) and in particular the KEs. The developed model is further compared with other three existing modeling approaches: LSTM-based, SVR-based, and polynomial-based models. The model quality is evaluated in terms of performance and computational costs. The achieved experimental-based findings demonstrate that the GRU-based model represents the optimal modeling choice and it allows achieving a great interpolation and extrapolation capability. The determined model is used to study the KEs in a systematic and numerical way without the need of extracting an equivalent-circuit representation. The application of the model for a straightforward analysis of the KEs is successfully validated with an experimental campaign of measurements, thereby enabling gaining a full assessment and deeper insights into the dependence of the KEs on the operating conditions. The rest of the paper is organized as follows. Section II introduces the modeling technique theory. Section III provides an extensive validation of the developed model. Section IV reports the analysis of the KEs in S_{22} and in h_{21} under different operating conditions by using the extracted model. Finally, conclusions are drawn in the final section.

II. BASIC THEORY OF MODELING TECHNOLOGY

Fig. 1 depicts a basic cell of the GRU networks. There are two gates to process the data: reset gate and update gate. The current input x_t and the previous state h_{t-1} are
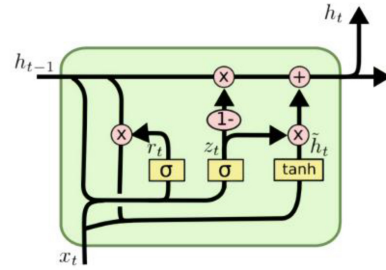
FIGURE 1. Illustration of the internal architecture of GRU cells. The symbols of "$\oplus$" and "$\otimes$" represent the operation of addition and element-wise multiplication, respectively.

processed together to calculate three gate parameters: r_t, z_t, and $\widetilde{h}_t$. Reset gate decides the $\widetilde{h}_t$ through combining the previous state h_{t-1} and input x_t and succeeds in memorizing present information. The update gate decides present state h_t, which leaves out unnecessary information and restores the information needed [36].

All calculation procedures can be depicted in the following equations:

a) Reset gate:

$$r_t = \sigma\left(W_r \cdot [x_t, \ h_{t-1}] + b_r\right) \tag{1}$$

$$h'_{t-1} = h_{t-1} \ \otimes \ r_t \tag{2}$$

$$\widetilde{h}_t = \tanh\left(W \cdot [\ h'_{t-1}, \ x_t] + b\right) \tag{3}$$

b) Update gate:

$$z_t = \sigma\left(W_z \cdot [x_t, \ h_{t-1}] + b_z\right) \tag{4}$$

c) State update:

$$h_t = z_t \otimes \widetilde{h}_t + (1 - \ z_t) \bigotimes \ h_{t-1} \tag{5}$$

where $\sigma(\cdot)$ represents the activation function, and W_r, W, and W_z represent weight matrices for r_t, $\widetilde{h}_t$, and z, respectively. Other parameters, like b_r, b, and b_z, are bias terms [36].
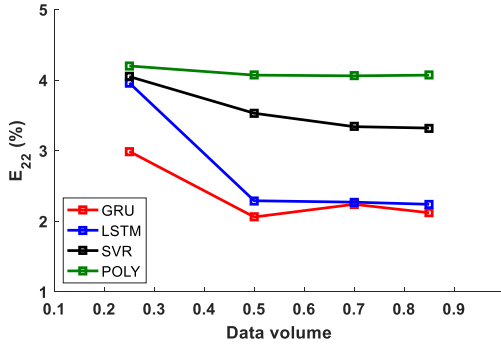
For the case of modeling S_{22}, the data are divided into two parts, namely the real and the imaginary parts. Therefore, the model training contains two separate processes. The input for the two cases of modeling S_{22} and h_{21} contains the information about bias point, frequency, and temperature. The model is built and trained using the Tensorflow platform, which is a very popular and powerful tool for constructing machine learning models. The transistor model is trained with the measured data, and optimized using the Nadam optimizer. With the training completed, the model can be used to predict the device performance. The task of comparing measurements with simulations is accomplished by implementing the developed model into the Keysight's ADS EDA tool.

III. DISCUSSION AND VALIDATION OF THE PROPOSED MODEL

This section is devoted to the validation of GRU-based model for S_{22} and h_{21} by using the measured data from 0.2 GHz

TABLE 1. Operating conditions used for model extraction.

Variables	Different States
V_{GS}	-3.1 V and -3.5 V
V_{DS}	0 V, 10 V, 20 V, and 30 V
T	35°C, 90°C, and 145°C

FIGURE 2. E_{22} **from different models versus training data usage.**

FIGURE 3. Measured (symbols), GRU modeled (black solid line), LSTM modeled (red dash line), SVR modeled (blue dot line), and polynomial modeled (green chain line) behavior of S_{22} for the studied GaN HEMT device at two different operating points (i.e., local conditions): (a) $V_{GS} = -3.1$ V and $V_{DS} = 20$ V with a temperature of 90°C and (b) $V_{GS} = -3.5$ V and $V_{DS} = 20$ V with a temperature of 145°C. The frequency range goes from 0.2 GHz to 65 GHz.

FIGURE 4. Measured (symbols), GRU modeled (black solid line), LSTM modeled (red dash line), SVR modeled (blue dot line), and polynomial modeled (green chain line) behavior of S_{22} for the studied GaN HEMT device at device at two different operating points (i.e., interpolation and extrapolation cases): (a) $V_{GS} = -3.13$ V and $V_{DS} = 30$ V with a temperature of 145°C (i.e., interpolation case) and (b) $V_{GS} = -3.5$ V and $V_{DS} = 20$ V with a temperature of 200°C (i.e., extrapolation case). The frequency range goes from 0.2 GHz to 65 GHz.
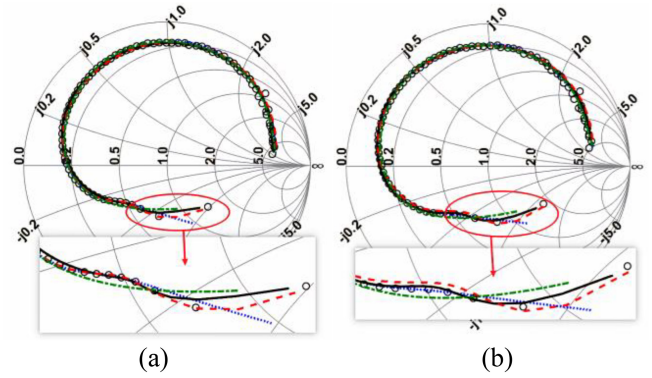
to 65 GHz with a step of 0.2 GHz for the tested 0.25x1500 μm^2 GaN HEMT on SiC. In order to determine which model has the superior fitting performance in reproducing S_{22}, the relative error E_{xy} is adopted as a metric of the model accuracy [37]. E_{xy} can be defined as follows:

$$E_{xy}\Big|_{y=1,2}^{x=1,2} = \sqrt{\frac{\sum_m \sum_n |S_{xy}^{sim} - S_{xy}^{meas}|^2}{\sum_m \sum_n |S_{xy}^{meas}|^2}} \qquad (6)$$
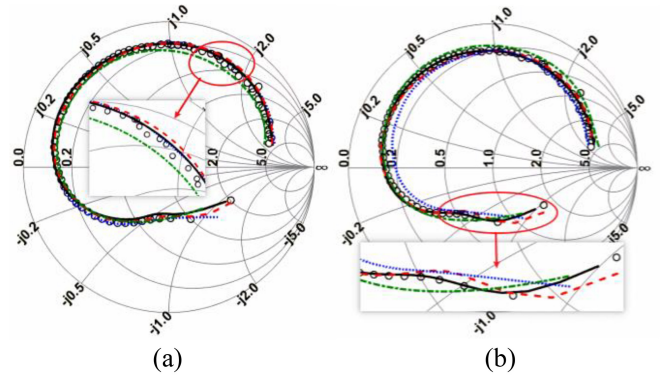
As part of the training process, two different bias conditions are used for V_{GS} (i.e., -3.1 V and -3.5 V) and each of them is combined with four different bias conditions for V_{DS} (i.e., 0 V, 10 V, 20 V, and 30 V). Each bias point is considered at three different ambient temperatures (i.e., 35°C, 90°C, and 145°C), resulting in 24 (i.e., 2*4*3=24) operating states totally. The details are shown in Table 1.

The volume of data used for model extraction is an important factor that impacts model performance. In this regard, data usage for model extraction must be considered before we test the proposed modeling method. As illustrated in Fig. 2, the proposed model is compared with the LSTM-based model, the SVR-based model, and the fifth-order polynomial-based model considering a temperature of 25°C and a bias condition of -3.5 V for V_{GS} and 20 V for V_{DS}. From the results, it can be seen that the performance of all models is generally enhanced with an increase in data usage for model extraction. As indicated in the figure, a 50% data usage for model extraction is a reasonable trade-off. Therefore, the remaining examples set model extraction data usage to 50%.

A detailed analysis of the prediction performance of the proposed model for S_{22} is presented in the following test case. The performance comparison is carried out using the same aforementioned models. The reported analysis has been conducted under "local" conditions (i.e., the tested condition is included in the model training), "inter" conditions (i.e., the

tested condition is an interpolated operating condition), and "extra" conditions (i.e., the tested condition is an extrapolated operating condition). As shown in Fig. 3, four modelling techniques were examined under two local conditions for modeling the behavior of S_{22}. Additionally, Fig. 4 compares four techniques for modeling the behavior of S_{22} under both inter- and extra-conditions. During the test, the operating conditions of the V_{GS} are interpolated for the "inter" test case, while the operating conditions of the temperature are extrapolated for the "extra" test case. As can be seen from the achieved results, the GRU-based model exhibits superior performance when compared with the other three models.

As shown in Table 2, the detailed relative error, E_{22}, is provided for each of the four models at four different operational scenarios. It is obvious that the GRU-based model shows a slight advantage over the LSTM-based model,

TABLE 2. Relative error of S$_{22}$ for different models.

Freq. (GHz)	Type	Operating Condition: (V_{GS}; V_{DS}; T)	E$_{22}$ (%)			
			GRU	LSTM	SVR	Poly
0.2-65	Local	-3.10 V; 20 V; 90°C	1.70	2.07	2.12	4.03
		-3.50 V; 20 V; 145°C	1.91	2.12	2.35	3.76
	Inter	-3.13 V; 30 V; 145°C	3.14	3.69	3.86	5.56
	Extra	-3.50 V; 20 V; 200°C	2.67	4.47	6.68	8.79

TABLE 3. Cost of different models.

| Model	Cost			
	Training Time (s)	Running Time (s)	Number of Parameters	Cell Number
GRU	240	0.078	111	5
LSTM	350	0.079	146	5
SVR	780	0.025	1502	/
Poly	0.034	0.011	6	/

but has a greater advantage over the SVR-based model and the polynomial-based model.

Table 3 provides a summary of the costs associated with the four different modeling techniques used in this study. As can be observed from this table, the polynomial-based model is much more efficient than the other three models, since it requires much less training time and parameters. However, if we take the model performance into consideration, the GRU-based model becomes the optimal modeling option. Fig. 5 illustrates the training loss versus epochs of both the GRU and LSTM models. In the test, the training loss is defined as the mean square error (MSE) of the models. When using the same number of epochs, the proposed method appears to have a lower loss than the LSTM model, thereby indicating that it is more efficient than the latter.

Table 4 shows E_{22} of GRU-based model with different activation functions. Three normal functions are adopted and compared. The interpolation and extrapolation capability of the proposed model with different bias conditions has also been validated. The model based on function of tanh shows best performance at all cases with lower and more stable values of E_{22}, which are all below 4.3%. Therefore, it has been clearly demonstrated that the developed model has great ability in fitting and predicting the behavior of S_{22}.

Fig. 6 shows the behavior of S_{22} at four operating points that are local conditions. Fig. 7(a) shows two interpolation test cases and Fig. 7(b) shows two extrapolation test cases. From these results, one can tell that the GRU-based model has a very general accurate fitting performance across the whole working frequency range.

In the following part of this section, the GRU-based model is used to predict the behavior of magnitude of h_{21}. The
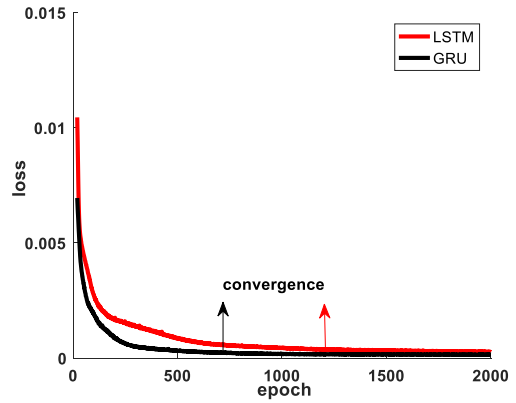
FIGURE 5. Training loss versus epochs for both the GRU (black) and LSTM (red) models.

TABLE 4. Relative error of S$_{22}$ from GRU model based on different activation functions.

| Freq. (GHz)	Type	Operating Condition: (V_{GS}; V_{DS}; T)	E$_{22}$ (%)		
			tanh	sig	relu
0.2-65	Local	-3.50 V; 20 V; 35°C	2.22	2.50	3.30
		-3.50 V; 10 V; 90°C	2.66	2.35	4.97
		-3.10 V; 20 V; 90°C	1.70	2.10	3.12
		-3.50 V; 20 V; 145°C	2.63	2.54	6.03
	Inter	-3.13 V; 30 V; 145°C	3.14	3.25	4.77
		-3.20 V; 30 V; 145°C	6.33	6.43	11.18
	Extra	-3.50 V; 20 V; 200°C	2.67	6.20	9.04
		-3.10 V; 10 V; 200°C	4.24	5.11	8.91
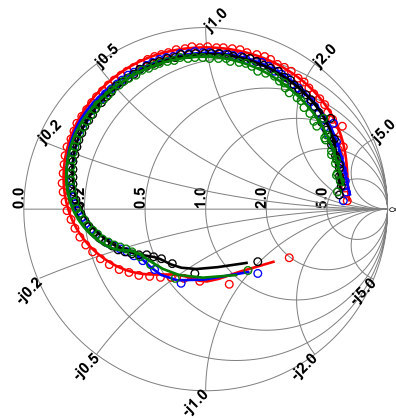
FIGURE 6. Measured (symbols) and modeled (lines) behavior of S_{22} for the studied GaN HEMT device at four different operating points (i.e., local conditions): V_{GS} = −3.5 V and V_{DS} = 20 V with a temperature of 35°C (red), V_{GS} = −3.5 V and V_{DS} = 10 V with a temperature of 90°C (blue), V_{GS} = −3.1 V and V_{DS} = 20 V with a temperature of 90°C (black), and V_{GS} = −3.5 V and V_{DS} = 20 V with a temperature of 145°C (green). The frequency range goes from 0.2 GHz to 65 GHz.

mean squared error (MSE) is adopted as a metric of the model accuracy, the equation is the following one:

$$MSE = \frac{1}{n} \sum_{i=1}^{n} (H_{meas} - H_{sim})^2 \qquad (7)$$

(a)   (b)
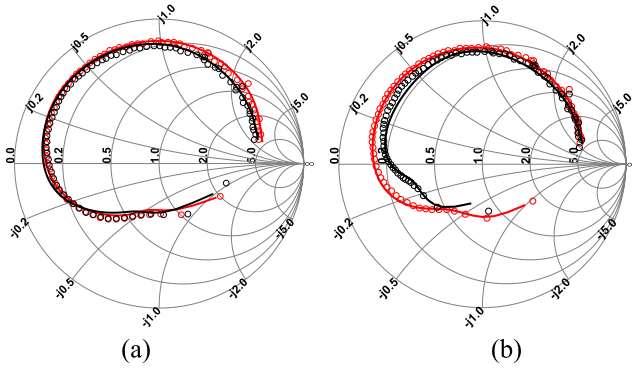
FIGURE 7. Measured (symbols) and modeled (lines) behavior of S_{22} for the studied GaN HEMT device at four different operating points: (a) V_{GS} = −3.13 V and V_{DS} = 30 V with a temperature of 145°C, −3.2 V and V_{DS} = 30 V with a temperature of 145°C (black) (i.e., interpolation case) and (b) V_{GS} = −3.5 V and V_{DS} = 20 V with a temperature of 200°C (red) and V_{GS} = −3.1 V and V_{DS} = 10 V with a temperature of 200°C (black) (i.e., extrapolation case). The frequency range goes from 0.2 GHz to 65 GHz.
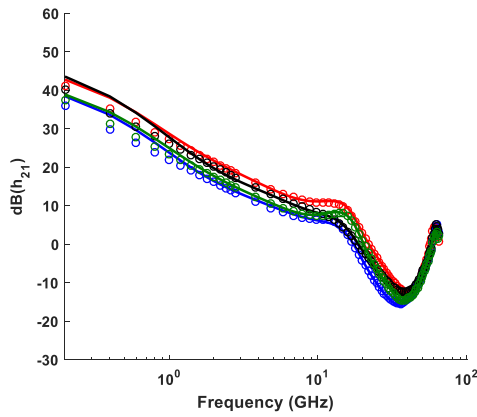
FIGURE 8. Measured (symbols) and modeled (lines) behavior of h_{21} for the studied GaN HEMT device at four different operating points (i.e., local conditions): V_{GS} = −3.1 V and V_{DS} = 20 V with a temperature of 35°C (red), V_{GS} = −3.5 V and V_{DS} = 10 V with a temperature of 90°C (blue), V_{GS} = −3.1 V and V_{DS} = 10 V with a temperature of 90°C (black), and V_{GS} = −3.5 V and V_{DS} = 20 V with a temperature of 145°C (green). The frequency range goes from 0.2 GHz to 65 GHz.

Fig. 8 shows the h_{21} at four operating points that are local conditions. Fig. 9(a) shows two interpolation test cases and Fig. 9(b) shows two extrapolation test cases. As can be seen, the model successfully predicts the general trend of h_{21} in both bias interpolation and extrapolation test cases.

Table 5 reports the MSE of GRU-based model for h_{21}. It can be learnt that such a kind of model provides the same level of accuracy for all the investigated conditions as indicated by the MSE values.

IV. ANALYSIS OF THE KES IN S22 AND H21

The methodology proposed in [13] is adopted in this study to characterize the size and shape of the KE in S_{22} by studying the D2 of the function $\mathrm{Im}(S_{22})$ versus $\mathrm{Re}(S_{22})$. In particular, the following kink parameters can be determined [13]:

1) The kink frequency band (KFB), which represents the frequency band between the start and the disappearance of

(a)   (b)
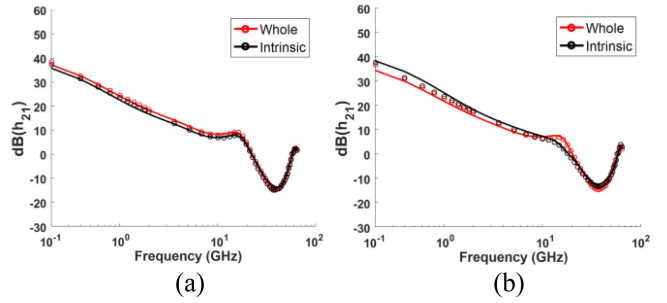
FIGURE 9. Measured (symbols) and modeled (lines) behavior of h_{21} for the studied GaN HEMT device at four different operating points: (a) V_{GS} = −3.13 V and V_{DS} = 30 V with a temperature of 145°C (red) and V_{GS} = −3.20 V and V_{DS} = 30 V with a temperature of 145°C (black) (i.e., interpolation case) and (b) V_{GS} = −3.5 V and V_{DS} = 20 V with a temperature of 200°C (red) and V_{GS} = −3.1 V and V_{DS} = 10 V with a temperature of 200°C (black) (i.e., extrapolation case). The frequency range goes from 0.2 GHz to 65 GHz.

TABLE 5. Mean squared error of magnitude of h_{21} in different cases.

Freq. (GHz)	Type	Operating Condition: (V_{GS}; V_{DS}; T)	MSE
0.2-65	Local	-3.10 V; 20 V; 35°C	2.7e-5
		-3.50 V; 10 V; 90°C	2.9e-5
		-3.10 V; 10 V; 90°C	2.0e-5
		-3.50 V; 20 V; 145°C	2.6e-5
	Inter	-3.20 V; 30 V; 145°C	7.9e-5
		-3.13 V; 30 V; 145°C	3.0e-5
	Extra	-3.50 V; 20 V; 200°C	5.7e-5
		-3.10 V; 10 V; 200°C	8.0e-5

TABLE 6. Extrinsic equivalent-circuit elements for the DUT.

T (°C)	35	90	145	200
C_{pg}, C_{pd} (fF)	80	80	80	80
L_g (pH)	76.7	76.0	75.9	75.4
L_s (pH)	9.6	9.5	9.6	10.2
L_d (pH)	79.1	78.0	77.1	76.6
R_g (Ω)	1.0	1.2	1.4	1.7
R_s (Ω)	0.4	0.4	0.4	0.4
R_d (Ω)	0.9	1.1	1.5	1.9

the KE, namely the band delimited by the two frequencies where the D2 becomes zero.

2) The kink frequency point (KFP), which represents the frequency where the KE is strongest, namely the frequency point where D2 has its negative peak value.

3) The kink size (KS), which represents the size of the KE, namely the value of the D2 at the KFP.

Table 6 shows the values of the extrinsic elements obtained from the previous work in [38], which have been successfully validated by the achieved good agreement between measurements and ECM stimulations. In the present study, the values of the extrinsic elements are used to access
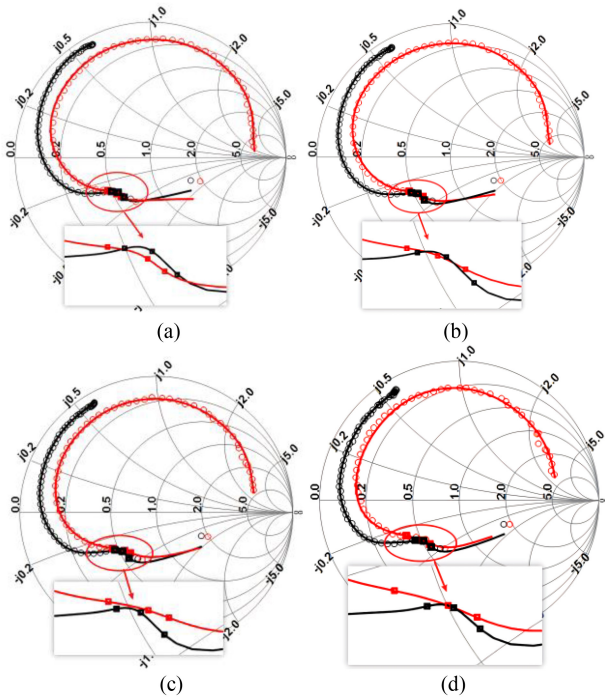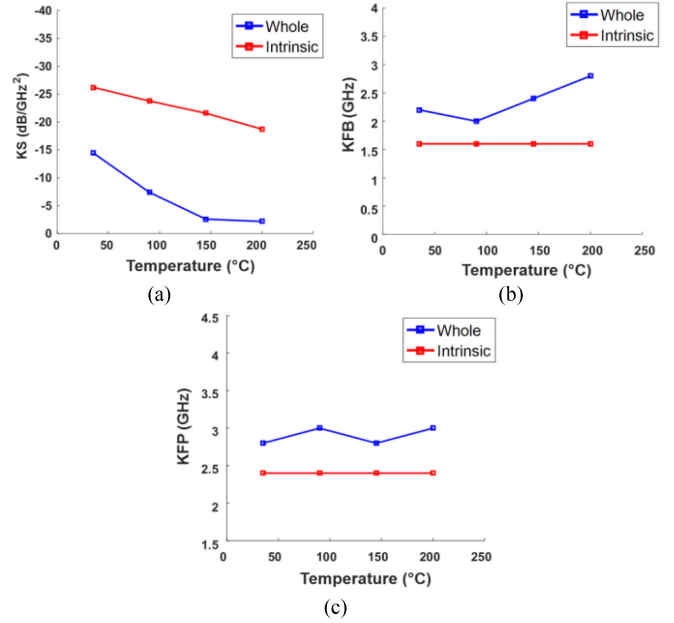
FIGURE 10. Measured (symbols) and modeled (lines) behavior of S_{22} for the whole (red) and intrinsic (black) GaN HEMT device at $V_{GS} = -3.1$ V and $V_{DS} = 20$ V under four different temperature conditions: (a) 35°C, (b) 90°C, (c) 145°C, and (d) 200°C. The frequency range goes from 0.2 GHz to 65 GHz. The four insets highlight the KE at each studied temperature by using three squares to represent the onset, peak, and disappearance of the KE in the modeled S_{22}.

FIGURE 11. Kink parameters for the KE in S_{22} versus ambient temperature for the whole (blue) and intrinsic (red) GaN HEMT device at $V_{GS} = -3.1$ V and $V_{DS} = 20$ V: (a) kink size, (b) kink frequency band, and (c) kink frequency point.

FIGURE 12. Modeled behavior of real part of Y_{21} at 0.2 GHz versus ambient temperature for the tested GaN HEMT device at different biases.
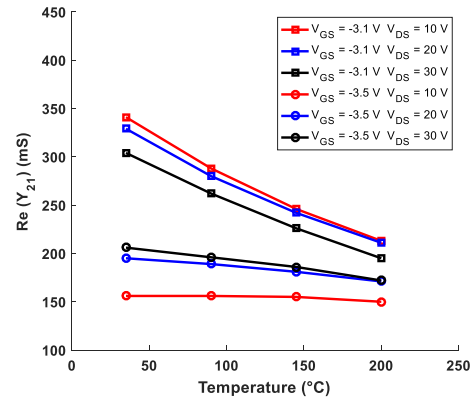
to the performance of the intrinsic device by applying the de-embedding procedure to both measurements and GRU-based simulations.

Fig. 10 illustrates the comparison between measured and modeled frequency-dependent behavior of S_{22} for the whole and intrinsic DUT. As can be clearly seen by the achieved good agreement between measurements and simulations, the GRU-based model has great fitting capability across the whole wide frequency range, thereby allowing its use for determining the D2 and then estimating the kink parameters. It should be underlined that Fig. 10 shows that the contributions of the extrinsic equivalent-circuit elements tend to mask the KE, which is more pronounced when considering only the intrinsic device as this effect is inherently rooted in the intrinsic section of the transistor.

Fig. 11 shows the temperature dependence of the kink parameters associated to the KE in S_{22} for both whole and intrinsic GaN HEMT devices. These kink parameters are calculated by using the simulations of GRU-based model that is able to accurately reproduce the measured S_{22}. From Fig. 11, it is clear that the ambient temperature is an important factor affecting the size and shape of the KE in S_{22}. With the variation of temperature, all kink parameters change correspondingly. In particular, Fig. 12 shows that, after de-embedding the extrinsic elements, the KE gets more pronounced, as can be quantified by the observed increase

in the magnitude of the kink size (see Fig. 11(a)), and, in addition, the KE affects the behavior in S_{22} into a smaller frequency range, as can be quantified by the observed change in the kink frequency band (see Fig. 11(b)).

Fig. 12 depicts the real part of the short-circuit forward transfer admittance (Y21) at low frequency versus temperature at different biases and it can be seen that such parameter deteriorates with the increase of temperature.

The observed decrease of the low-frequency $Re(Y_{21})$ with increasing temperature can be attributed to the fact that this parameter is strongly linked to intrinsic transconductance [26], which decreases at higher temperatures because of the degradation of the electron transport properties. This result should lead to a less severe KE at higher temperature and, then, to a reduction in the magnitude of the KS,
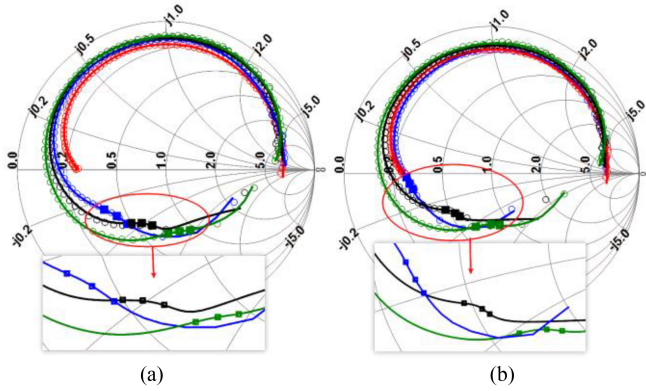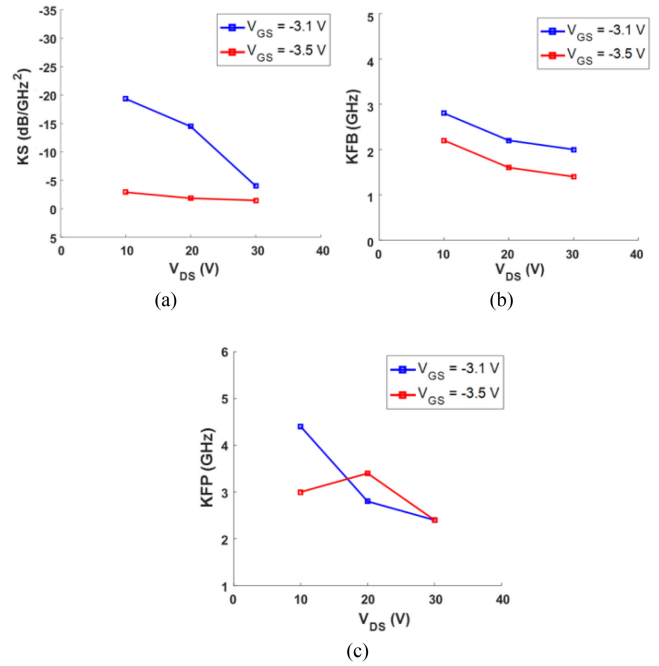
FIGURE 13. Measured (symbols) and modeled (lines) behavior of S_{22} at different bias conditions with a temperature of 35°C: (a) fixed $V_{GS} = -3.1$ V and $V_{DS} = 0$ V for bias1 (red), $V_{DS} = 10$ V for bias2 (blue), $V_{DS} = 20$ V for bias3 (black), and $V_{DS} = 30$ V for bias4 (green), (b) fixed $V_{GS} = -3.5$ V and $V_{DS} = 0$ V for bias5 (red), $V_{DS} = 10$ V for bias6 (blue), $V_{DS} = 20$ V for bias7 (black), and $V_{DS} = 30$ V for bias8 (green). The frequency range goes from 0.2 GHz to 65 GHz. The two insets highlight the KE by using three squares on each temperature case to represent the onset, peak, and disappearance of the KE in the modeled S_{22}.

since the KE in S_{22} is mostly due to the relatively high intrinsic transconductance. In line with this observation, by focusing the attention on the kink size, it can be seen that the KE has a clear trend of becoming less pronounced with the temperature getting higher, as can be detected by the observed reduction in the magnitude of the KS (see Fig. 11(a)).

As can be clearly observed from Fig. 13, the GRU-based model exhibits great fitting performance for prediction the behavior of S_{22} under different bias conditions. It should be underlined that the kink effect disappears at $V_{DS} = 0$ V (see Fig. 13). This is because of the zero g_m, since this parameter, as previously discussed, is the main reason for the appearance of the KE in S_{22}.

Fig. 14 shows the bias dependence of the kink parameters associated to the KE in S_{22} for whole GaN HEMT device. Fig. 15 tells that the chosen bias point is an important factor affecting the size and shape of the KE in S_{22}. In fact, by lowering V_{GS} from -3.1 V to -3.5 V, the KE becomes less pronounced, which is testified by the observed decrease in the magnitude of the kink size (see Fig. 14(a)). This can be attributed to the reduction of the intrinsic g_m, which can be seen in the reduction of the low-frequency $Re(Y_{21})$ (see Fig. 12). Similarly, the magnitude of the KS is reduced by increasing V_{DS} from 10 V to 30 V with $V_{GS} = -3.1$ V, which is in line with the observed reduction of the low-frequency $Re(Y_{21})$ (see Fig. 12). On the other hand, the magnitude of the KS is reduced by increasing V_{DS} from 10 V to 30 V with $V_{GS} = -3.5$ V even if an increase in the low-frequency $Re(Y_{21})$ is observed (see Fig. 15). This finding might be due to the fact that, although g_m has a strong impact on the KE, this phenomenon is the result from the combined effect of the values of the all equivalent-circuit elements.
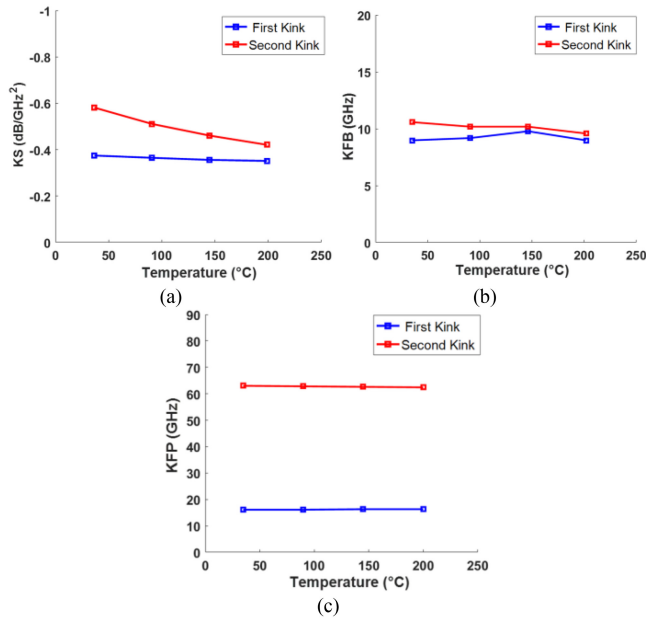

FIGURE 14. Kink parameters for the KE in S_{22} versus V_{DS} for the studied GaN HEMT device at $V_{GS} = -3.1$ V (blue) and $V_{GS} = -3.5$ V (red): (a) kink size, (b) kink frequency band, and (c) kink frequency point.
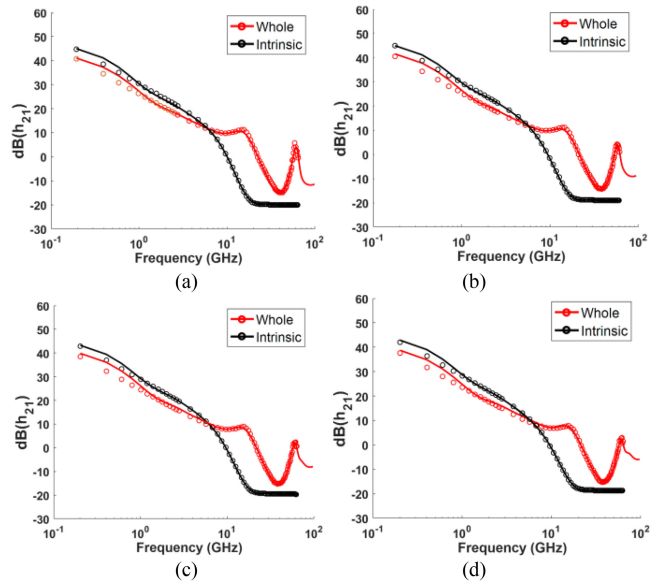
FIGURE 15. Measured (symbols) and modeled (lines) behavior of the magnitude of h_{21} for the whole (red) and intrinsic (black) GaN HEMT device at $V_{GS} = -3.1$ V and $V_{DS} = 30$ V under four different temperature conditions: (a) 35°C, (b) 90°C, (c) 145°C, and (d) 200°C. The frequency range goes from 0.2 GHz to 65 GHz, and that of modeled whole device is extended to 100 GHz.

As can be clearly seen from Fig. 15, the GRU-based model exhibits a level of accuracy in the prediction of h_{21}. In fact, it can accurately capture the frequency-dependent behavior of h_{21}, including the observed peaks and their variations with the change of temperature. It should be noticed that, to get the kink parameters of the second peak, the proposed model

FIGURE 16. Kink parameters for the two KEs in h_{21} versus ambient temperature for the studied GaN HEMT device at $V_{GS} = -3.1$ V and $V_{DS} = 30$V: (a) kink size, (b) kink frequency band, and (c) kink frequency point.

FIGURE 17. Measured (symbols) and modeled (lines) behavior of the magnitude of h_{21} with a temperature of 145°C, at (a) fixed $V_{GS} = -3.1$ V and $V_{DS} = 0$ V for bias1 (red), $V_{DS} = 10$ V for bias2 (blue), $V_{DS} = 20$ V for bias3 (black) and $V_{DS} = 30$ V for bias4 (green), (b) fixed $V_{GS} = -3.5$ V and $V_{DS} = 0$ V for bias5 (red), $V_{DS} = 10$ V for bias6 (blue), $V_{DS} = 20$ V for bias7 (black), and $V_{DS} = 30$ V for bias8 (green). The frequency range goes from 0.2 GHz to 65 GHz and that of modeled whole device is extended up to 100 GHz.

is extrapolated up to 100 GHz, since the frequency band of the second peak extends beyond the upper frequency limit of the available experiments (i.e., 65 GHz), thereby allowing an accurate determination of the kink parameters associated to the two observed peaks (see Fig. 16 and Fig. 18). Fig. 15 shows that, after applying the de-embedding of the extrinsic elements, both peaks in the magnitude of h_{21} disappear. This finding is consistent with the fact that the two peaks arise from the combined effects of both intrinsic and extrinsic elements. As a matter of fact, the first and the second peaks in h_{21} have been ascribed to the resonance between the extrinsic inductances and the intrinsic capacitances and to the resonance between the extrinsic inductances and the extrinsic capacitances, respectively [17], [26].

Likewise to the case of S_{22}, the three kink parameters KFB, KFP, and KS can be defined for h_{21} by using the D2 for the function of h_{21} expressed in dB versus frequency [26]. In the case of h_{21}, the kink parameters can be evaluated only for the whole device, since, as said, both peaks in the magnitude of h_{21} disappear after applying the de-embedding of the extrinsic contributions. These kink parameters are calculated by using the simulations of GRU-based model that is able to reproduce accurately the measured h_{21}. Fig. 16 shows the temperature dependence of the kink parameters associated to both KEs in h_{21} for the DUT. As can be observed, the temperature has a little impact on the two peaks in h_{21}. It should be highlighted that the two KFPs associated to the two peaks are substantially insensitive to the temperature (see Fig. 16 (c)), which is in line with the fact that the two resonant frequencies are associated to elements (i.e., extrinsic inductances, extrinsic
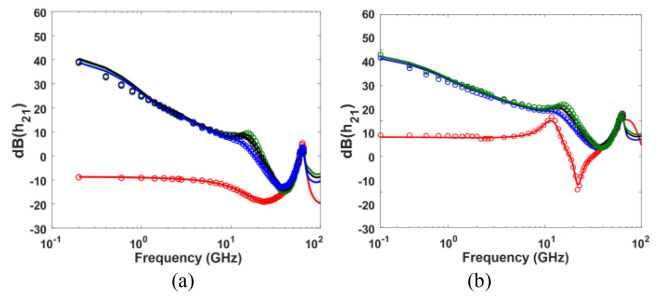
capacitances, and intrinsic capacitances) that are mostly temperature insensitive.

Fig. 17 shows that the developed model is able to reproduce accurately the behavior of the magnitude of h_{21} under different bias conditions. Likewise to what was done in Fig. 15, the frequency range of the simulations has been extended up to 100 GHz. By analyzing the condition $V_{DS} = -3.1$ V and $V_{DS} = 0$ V, it is observed that the first kink in h_{21} disappears, due to the high value of the intrinsic g_{ds} that tends to short circuit the contributions of the intrinsic capacitances on Z_{22}, while the second kink in h_{21} is still there, confirming that this effect is due to extrinsic contributions that are bias independent [27]. It is found that the first kink in h_{21} occurs when analyzing the condition $V_{GS} = -3.5$ V and $V_{DS} = 0$ V. This is because when moving towards the pinch-off condition by lowering V_{GS} from -3.1 V to -3.5 V, the value of the intrinsic g_{ds} is reduced significantly. As a matter of fact, Fig. 19 depicts the real part of the short-circuit output admittance (Y_{22}) at low frequency versus V_{DS} at $V_{GS} = -3.1$ V and $V_{GS} = -3.5$ V with a temperature of 145°C. As can be clearly seen, such parameter is remarkably decreased by lowering V_{GS} from -3.1 V to -3.5 V. This observed decrease of the low-frequency Re(Y_{22}) can be attributed to the fact that this parameter is strongly linked to intrinsic output conductance [26], which decreases when moving towards to the pinch-off.

Compared to the ambient temperature that has a little impact on the KEs in h_{21}, the bias condition plays a more pronounced role in determining the values of the kink parameters associated to the KEs in h_{21} (see Fig. 18). However, as can be observed from Fig. 18(c), the KFP associated to the first peak, which arises from the resonance between the extrinsic inductances and the intrinsic capacitances, depends slightly on the bias condition, due to the weak variations of the intrinsic capacitances in the considered bias region, and the KFP associated to the second peak, which arises from the resonance between the extrinsic inductances and the extrinsic capacitances, is substantially insensitive to the bias condition, owing to the bias independence of the extrinsic reactive elements.
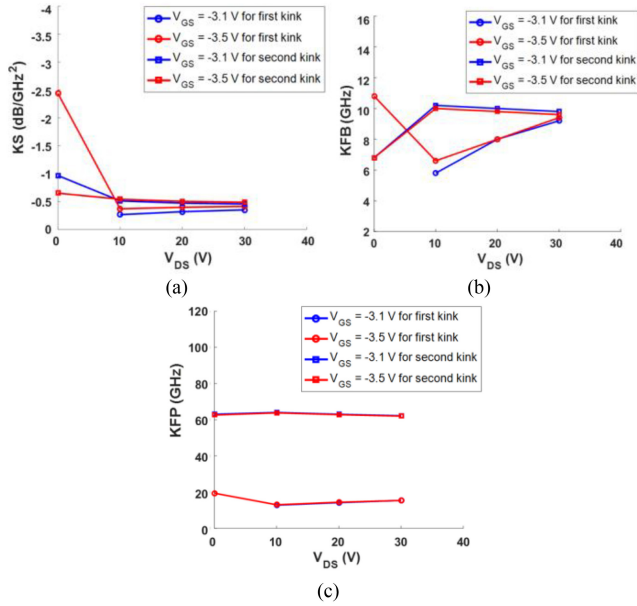
FIGURE 18. Kink parameters for the two KEs in h_{21} versus V_{DS} for the studied GaN HEMT device at $V_{GS} = -3.1$ V (blue) and $V_{GS} = -3.5$ V (red) with a temperature of 145°C: (a) kink size, (b) kink frequency band, and (c) kink frequency point.
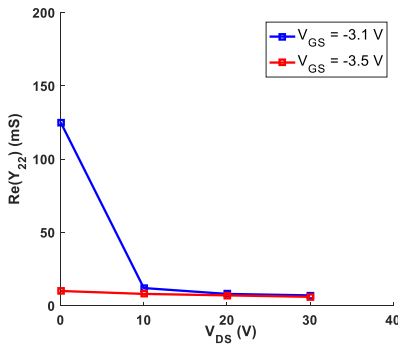
FIGURE 19. Behavior of real part of Y_{22} at 0.2 GHz versus V_{DS} for the tested GaN HEMT device at $V_{GS} = -3.1$ V and $V_{GS} = -3.5$ V with a temperature of 145°C.

V. CONCLUSION

Both anomalous kinks in S_{22} and in h_{21} for a GaN HEMT device are deeply analyzed using *S*-parameter measurements performed under different bias points with the operating frequency going up to 65 GHz and the ambient temperature increased up to 200°C. A modeling technique based on GRU, which consists of a modified RNN, is here exploited for the first time to accurately investigate the KEs, with the aim of definitely clarifying some assumptions discussed in literature. The test results show that GRU-based model with tanh served as activation function owns great fitting performance for the behavior modeling of S_{22} and h_{21}. Both the interpolation and extrapolation capability of the achieved model are tested, and it exhibits great prediction ability. The developed study has confirmed that the KE in S_{22} is inherently rooted in the intrinsic device and it becomes less pronounced when considering also the contributions

of the extrinsic circuit elements. On the other hand, both peaks in h_{21} expressed in dB disappear after de-embedding of the extrinsic elements as they play a key role in the appearance of the two peaks. In particular, the first and the second peaks in h_{21} arise from the resonance between the extrinsic inductances and the intrinsic capacitances and to the resonance between the extrinsic inductances and the extrinsic capacitances, respectively. In addition, it is shown that the temperature has a more pronounced effect in the KE in S_{22} rather than in the KEs in h_{21}, while all of the three KEs can be strongly affected by the selected bias condition.

REFERENCES

[1] C. Florian, F. Mastri, R. P. Paganelli, D. Masotti, and A. Costanzo, "Theoretical and numerical design of a wireless power transmission link with GaN-based transmitter and adaptive receiver," *IEEE Trans. Microw. Theory Techn.*, vol. 62, no. 4, pp. 931–946, Apr. 2014, doi: 10.1109/TMTT.2014.2303949.

[2] R. Giofrè, P. Colantonio, F. Costanzo, F. Vitobello, M. Lopez, and L. Cabria, "A 17.3–20.2-GHz GaN-Si MMIC balanced HPA for very high throughput satellites," *IEEE Microw. Wireless Compon. Lett.*, vol. 31, no. 3, pp. 296–299, Mar. 2021, doi: 10.1109/LMWC.2020.3047211.

[3] R. S. Pengelly, S. M. Wood, J. W. Milligan, S. T. Sheppard, and W. L. Pribble, "A review of GaN on SiC high electron-mobility power transistors and MMICs," *IEEE Trans. Microw. Theory Techn.*, vol. 60, no. 6, pp. 1764–1783, Jun. 2012, doi: 10.1109/TMTT.2012.2187535.

[4] A. Jarndal and G. Kompa, "An accurate small-signal model for AlGaN-GaN HEMT suitable for scalable large-signal model construction," *IEEE Microw. Wireless Comp. Lett.*, vol. 16, no. 6, pp. 406–408, Jun. 2006, doi: 10.1109/LMWC.2006.875626.

[5] S.-S. Lu, C. Meng, T.-W. Chen, and H.-C. Chen, "A novel interpretation of transistor S-parameters by poles and zeros for RF IC circuit design," *IEEE Trans. Microw. Theory Techn.*, vol. 49, no. 2, pp. 406–409, Feb. 2001, doi: 10.1109/22.903109.

[6] H. Hjelmgren and A. Litwin, "Small-signal substrate resistance effect in RFCMOS identified through device simulations," *IEEE Trans. Electron Dev.*, vol. 48, no. 2, pp. 397–399, Feb. 2001, doi: 10.1109/16.902747.

[7] S. Lee et al., "An X-band GaN HEMT power amplifier design using an artificial neural network modeling technique," *IEEE Trans. Electron Dev.*, vol. 48, no. 3, pp. 495–501, Mar. 2001, doi: 10.1109/16.906442.

[8] Y.-S. Lin, "Analysis of RF scattering parameters and noise and power performances of RF-power MOS in 0.15-μm RF CMOS technology for RF SOC applications," *Microw. Opt. Tech. Lett.*, vol. 41, no. 3, pp. 191–196, May 2004, doi: 10.1002/mop.20089.

[9] Y.-S. Lin, "An analysis of small-signal source-body resistance effect on RF MOSFETs for low-cost system-on-chip (SoC) applications," *IEEE Trans. Electron Dev.*, vol. 52, no. 7, pp. 1442–1451, Jul. 2005, doi: 10.1109/TED.2005.850691.

[10] J. Shohat, I. D. Robertson, and S. J. Nightingale, "Investigation of drain-line loss and the S_{22} kink effect in capacitively coupled distributed amplifiers," *IEEE Trans. Microw. Theory Techn.*, vol. 53, no. 12, pp. 3767–3773, Dec. 2005, doi: 10.1109/TMTT.2005.859873.

[11] S.-S. Lu, C. Meng, T.-W. Chen, and H.-C. Chen, "The origin of the kink phenomenon of transistor scattering parameter S_{22}," *IEEE Trans. Microw. Theory Techn.*, vol. 49, no. 2, pp. 333–340, Feb. 2001, doi: 10.1109/22.903094.

[12] H. Gao, X. Sun, Y. Hua, X. Zhang, R. Wang, and G. P. Li, "A composite transistor to suppress kink phenomenon in HBTs for broadband design," *IEEE Electron Dev. Lett.*, vol. 31, no. 10, pp. 1113–1115, Oct. 2010, doi: 10.1109/LED.2010.2057240.

[13] G. Crupi, A. Raffo, A. Caddemi, and G. Vannini, "The kink phenomenon in the transistor S_{22}: A systematic and numerical approach," *IEEE Microw. Wirel. Compon. Lett.*, vol. 22, no. 8, pp. 406–408, Aug. 2012, doi: 10.1109/LMWC.2012.2205232.

[14] G. Crupi et al., "An extensive experimental analysis of the kink effects in S_{22} and h_{21} for a GaN HEMT," *IEEE Trans. Microw. Theory Techn.*, vol. 62, no. 3, pp. 513–520, Mar. 2014, doi: 10.1109/TMTT.2014.2299769.

[15] G. Crupi, A. Raffo, A. Caddemi, and G. Vannini, "Kink effect in S_{22} for GaN and GaAs HEMTs," *IEEE Microw. Wirel. Compon. Lett.*, vol. 25, no. 5, pp. 301–303, May 2015, doi: 10.1109/LMWC.2015.2409989.

[16] S. A. Ahsan, S. Ghosh, S. Khandelwal, and Y. S. Chauhan, "Modeling of kink-effect in RF behaviour of GaN HEMTs using ASM-HEMT model," in *Proc. IEEE Int. Conf. Electron Devices Solid State Circuits*, Hong Kong, China, 2016, pp. 426–429, doi: 10.1109/EDSSC.2016.7785299.

[17] G. Crupi, A. Raffo, V. Vadalà, G. Vannini, and A. Caddemi, "A new study on the temperature and bias dependence of the kink effects in S_{22} and h_{21} for the GaN HEMT technology," *Electronics*, vol. 7, no. 12, p. 353, Dec. 2018, doi: 10.3390/electronics7120353.

[18] M. A. Alim, A. A. Rezazadeh, C. Gaquiere, and G. Crupi, "Thermal influence on S_{22} kink behavior of a 0.15-μm gate length AlGaN/GaN/SiC HEMT for microwave applications," *Semicond. Sci. Technol.*, vol. 34, no. 3, pp. 1–8, Mar. 2019, doi: 10.1088/1361-6641/aafc78.

[19] G. Crupi, A. Raffo, Z. Marinković, D. M. M.-P. Schreurs, and A. Caddemi, "A comprehensive and critical overview of the kink effect in S_{22} for HEMT technology," in *Proc. IEEE Int. Conf. Adv. Technol., Syst. Services Telecommun. (TELSIKS)*, Nis, Serbia, 2019, pp. 13–20, doi: 10.1109/TELSIKS46999.2019.9002127.

[20] S. Osmanoglu and E. Ozbay, "Effect of the gate structure on the kink phenomenon in S_{22} of AlGaN/GaN HEMT," *Electron. Lett.*, vol. 57, no. 3, pp. 139–141, Feb. 2021, doi: 10.1049/ell2.12074.

[21] S. H. Meng et al., "Electron radiation impact on the kink effect in S_{22} of InP-based high electron mobility transistors," *Semicond. Sci. Technol.*, vol. 36, no. 9, Sep. 2021, Art. no. 095029, doi: 10.1088/1361-6641/ac0e76.

[22] Z. Zhu, M. Geng, J. Cai, and H. Gao, "Analysis and modeling of the kink effect in S_{22} based on support vector machine for GaN HEMTs," *Int. J. Numer. Model. Electron. Netw. Dev. Field*, vol. 35, no. 4, Jul./Aug. 2022, Art. no. e2992.

[23] G. Crupi, A. Raffo, D. M. M.-P. Schreurs, G. Avolio, A. Caddemi, and G. Vannini, "A clear-cut understanding of the current-gain peak in HEMTs: Theory and experiments," *Microw. Opt. Tech. Lett.*, vol. 54, no. 12, pp. 2801–2806, Dec. 2012, doi: 10.1002/mop.27192.

[24] G. Crupi, A. Raffo, D. M. M.-P. Schreurs, G. Avolio, A. Caddemi, and G. Vannini, "Identification of the intrinsic capacitive core for GaAs HEMTs by investigating the frequency behavior of the impedance parameters," *Microw. Opt. Tech. Lett.*, vol. 55, no. 6, pp. 1237–1240, Jun. 2013, doi: 10.1002/mop.27544.

[25] S. A. Ahsan, S. Ghosh, S. Khandelwal, and Y. S. Chauhan, "Pole-zero approach to analyze and model the kink in gain-frequency plot of GaN HEMTs," *IEEE Microw. Wirel. Compon. Lett.*, vol. 27, no. 3, pp. 266–268, Nov. 2017, doi: 10.1109/LMWC.2017.2661710.

[26] G. Crupi et al., "Technology-independent analysis of the double current-gain peak in millimeter-wave FETs," *IEEE Microw. Wirel. Compon. Lett.*, vol. F28, no. 4, pp. 326–328, Apr. 2018, doi: 10.1109/LMWC.2018.2808418.

[27] M. A. Alim, M. A. Hasan, A. A. Rezazadeh, C. Gaquiere, and G. Crupi, "Multi-bias and temperature dependence of the current-gain peak in GaN HEMT," *Int. J. RF Microw. Comput. Aided Eng.*, vol. 30, no. 4, Apr. 2020, Art. no. e22129, doi: 10.1002/mmce.22129.

[28] P. K. Kaushik et al., "Simulation-based study of current gain peaks h_{21} at low gate bias in AlGaN/GaN HEMTs" *Eng. Res. Exp.*, vol. 4, no. 2, 2022, Art. no. 025042, doi: 10.1088/2631-8695/ac743b.

[29] J. Cai, J. King, and J. C. Pedro, "A new nonlinear behavioral modeling technique for RF power transistors based on Bayesian inference," in *Proc. IEEE MTT-S Int. Microw. Symp. Dig.*, Honolulu, USA, 2017, pp. 624–626, doi: 10.1109/MWSYM.2017.8058645.

[30] M. Geng, J. Cai, C. Yu, J. Su, and J. Liu, "Piecewise small signal behavioral model for GaN HEMTs based on support vector regression," in *Proc. IEEE MTT-S Int. Conf. Numer. Electrom. Multiphys. Model. Optim. (NEMO)*, Hangzhou, China, 2022, pp. 1–3, doi: 10.1109/NEMO49486.2020.9343555.

[31] A. Khusro, M. S. Hashmi, and A. Q. Ansari, "Enabling the development of accurate intrinsic parameter extraction model for GaN HEMT using support vector regression (SVR)," *IET Microw. Antennas Propag.*, vol. 13, no. 9, pp. 1457–1466, Jul. 2019, doi: 10.1049/iet-map.2018.6039.

[32] J. Cai, C. Yu, L. Sun, S. Chen, and J. B. King, "Dynamic behavioral modeling of RF power amplifier based on time-delay support vector regression," *IEEE Trans. Microw. Theory Techn.*, vol. 67, no. 2, pp. 533–543, Feb. 2019, doi: 10.1109/TMTT.2018.2884414.

[33] M. H. Weatherspoon, H. A. Martinez, D. Langoni, and S. Y. Foo, "Small-signal modeling of microwave MESFETs using RBF-ANNs," *IEEE Trans. Instrum. Meas.*, vol. 56, no. 5, pp. 2067–2072, Oct. 2007, doi: 10.1109/TIM.2007.895585.

[34] P. Chen, S. Alsahali, A. Alt, J. Lees, and P. J. Tasker, "Behavioral modeling of GaN power amplifiers using long short-term memory networks," in *Proc. Int. Workshop Integr. Nonlin. Microw. Millimetre-Wave Circuits (INMMIC)*, Brive La Gaillarde, France, 2018, pp. 1–3, doi: 10.1109/INMMIC.2018.8429984.

[35] S. Hochreiter and J. Schmidhuber, "Long short-term memory," *Neural Comput.*, vol. 9, no. 8, pp. 1735–1780, Nov. 1997, doi: 10.1162/neco.1997.9.8.1735.

[36] J. Chung, C. Gulcehre, and K. H. Cho, "Empirical evaluation of gated recurrent neural networks on sequence modeling," 2014, *arXiv.1412.3555.*

[37] A. Raffo, J. Lonac, D. Resca, S. Monaco, A. Santarelli, and G. Vannini, "Comparison of electron device models based on operation-specific metrics," in *Proc. Asia Pac. Microw. Conf.*, 2005, pp.1–4, doi: 10.1109/APMC.2005.1606820.

[38] G. Crupi, A. Raffo, V. Vadalà, G. Vannini, and A. Caddemi, "High-periphery GaN HEMT modeling up to 65 GHz and 200°C," *Solid State Electron.*, vol. 152, pp. 11–16, Feb. 2019, doi: 10.1016/j.sse.2018.11.006.